1-1-2009

Periodic Radio and H Alpha Emission From The L Dwarf Binary 2massw J0746425 + 200032: Exploring The Magnetic Field Topology And Radius Of An L Dwarf

E. Berger

R. E. Rutledge

N. Phan-Bao

G. Basri

M. S. Giampapa

The Astrophysical Journal, 695:310–316, 2009 April 10 doi:10.1088/0004-637X/695/1/310

PERIODIC RADIO AND Hα EMISSION FROM THE L DWARF BINARY 2MASSW J0746425+200032: EXPLORING THE MAGNETIC FIELD TOPOLOGY AND RADIUS OF AN L DWARF

E. Berger[1], R. E. Rutledge[2], N. Phan-Bao[3], G. Basri[4], M. S. Giampapa[5], J. E. Gizis[6], J. Liebert[7], E. Martín[8,9], and T. A. Fleming[7]

[1] Harvard-Smithsonian Center for Astrophysics, 60 Garden Street, Cambridge, MA 02138, USA
[2] Department of Physics, McGill University, 3600 University Street, Montreal, QC H3A 2T8, Canada
[3] Institute of Astronomy and Astrophysics, Academia Sinica, P.O. Box 23-141, Taipei 10617, Taiwan
[4] Astronomy Department, University of California, Berkeley, CA 94720, USA
[5] National Solar Observatory, National Optical Astronomy Observatories, Tucson, AZ 85726, USA
[6] Department of Physics and Astronomy, University of Delaware, Newark, DE 19716, USA
[7] Department of Astronomy and Steward Observatory, University of Arizona, 933 North Cherry Avenue, Tucson, AZ 85721, USA
[8] Instituto de Astrofísica de Canarias, C/ Vía Láctea s/n, E-38200 La Laguna, Tenerife, Spain
[9] University of Central Florida, Department of Physics, PO Box 162385, Orlando, FL 32816, USA
Received 2008 September 2; accepted 2009 January 14; published 2009 March 30

ABSTRACT

We present an 8.5 hr simultaneous radio, X-ray, UV, and optical observation of the L dwarf binary 2MASSW J0746425+200032. We detect strong radio emission, dominated by short-duration periodic pulses at 4.86 GHz with $P = 124.32 \pm 0.11$ min. The stability of the pulse profiles and arrival times demonstrates that they are due to the rotational modulation of a $B \approx 1.7$ kG magnetic field. A quiescent nonvariable component is also detected, likely due to emission from a uniform large-scale field. The Hα emission exhibits identical periodicity, but unlike the radio pulses it varies sinusoidally and is offset by exactly 1/4 of a phase. The sinusoidal variations require chromospheric emission from a large-scale field structure, with the radio pulses likely emanating from the magnetic poles. While both light curves can be explained by a rotating misaligned magnetic field, the 1/4 phase lag rules out a symmetric dipole topology since it would result in a phase lag of 1/2 (poloidal field) or zero (toroidal field). We therefore conclude that either (1) the field is dominated by a quadrupole configuration, which can naturally explain the 1/4 phase lag; or (2) the Hα and/or radio emission regions are not trivially aligned with the field. Regardless of the field topology, we use the measured period along with the known rotation velocity ($v \sin i \approx 27$ km s^{-1}), and the binary orbital inclination ($i \approx 142^{\circ}$), to derive a radius for the primary star of 0.078 ± 0.010 $R_{\odot}$. This is the first measurement of the radius of an L dwarf, and along with a mass of 0.085 ± 0.010 $M_{\odot}$ it provides a constraint on the mass–radius relation below 0.1 $M_{\odot}$. We find that the radius is about 30% smaller than expected from theoretical models, even for an age of a few Gyr. The origin of this discrepancy is either a breakdown of the models at the bottom of the main sequence, or a significant misalignment between the rotational and orbital axes.

Key words: radio continuum: stars – stars: activity – stars: low-mass, brown dwarfs – stars: magnetic fields

Online-only material: color figures

1. INTRODUCTION

Radio observations conducted over the past several years have shown that about 10% of all very low-mass stars and brown dwarfs of spectral types M7–L3 are magnetically active (Berger 2006). Both quiescent and flaring emission are present, with luminosities that remain unchanged down to at least spectral type ∼ L3, in contrast to the declining activity seen in X-rays and Hα (Berger et al. 2001, 2005, 2008a, 2008b; Berger 2002, 2006; Burgasser & Putman 2005; Osten et al. 2006; Hallinan et al. 2006, 2007, 2008; Antonova et al. 2007, 2008; Phan-Bao et al. 2007; Audard et al. 2007). Depending on the nature of the radio emission mechanism, the inferred magnetic field strengths are ∼ 0.1–3 kG with order unity filling factors (Berger 2006; Hallinan et al. 2008). Long term monitoring of several objects in the spectral type range M8–L3.5 has further shown that the fields are generally stable for at least several years (Berger et al. 2005, 2008a; Berger 2006; but see also Antonova et al. 2007), providing an important constraint on the lifetime of magnetic dynamos in fully convective objects. The strength, scale, and stability of the inferred fields are in good agreement with recent results from phase-resolved spectropolarimetry (spectral type ∼ M4; Donati et al. 2006; Morin et al. 2008) and Zeeman broadening of FeH lines (spectral type < M9; Reiners & Basri 2006, 2007), as well as with the most recent numerical dynamo simulations (e.g., Browning 2008).

Equally important, three ultracool dwarfs to date have been observed to produce periodic radio emission, with periods of 184 min (2MASS J00361617+1821104; Berger et al. 2005), 118 min (TVLM 513−46546[10]; Hallinan et al. 2007), and 170 min (LSR 1835+3259; Hallinan et al. 2008). In the case of 2M 0036+18, the periodic emission is sinusoidal, while in the latter two objects it is in the form of short-duration pulses (duty cycle of a few percent). In all three cases, the observed periods are in good agreement with the known rotation velocities ($v \sin i$), indicating that the radio periodicity traces the stellar rotation.

As a result, in addition to allowing a measurement of the magnetic field properties, radio observations provide a unique opportunity to measure the radii of late-M and L dwarfs through the combination of rotation period and velocity. However, since only $v \sin i$ values are known for these objects, there is an inherent degeneracy between the radius and the inclination of

[10] This object also exhibits periodic Hα emission, with the same period as observed in the radio (Berger et al. 2008a).

the rotation axis, i. Using a typical range of $R \approx 0.09$–$0.11\ R_\odot$ for late-M and L dwarfs, the allowed range of inclinations span a relatively wide range of ~ 60–90° (Berger et al. 2005; Hallinan et al. 2008). To break this degeneracy, and thus measure the radius directly, it is desirable to observe objects for which the inclination can be estimated. This is the case for binary systems with well determined orbital parameters if we make the reasonable assumption that the rotation and orbital axes are aligned (Hale 1994). Along with an estimate of the mass, we can thus place constraints on the mass–radius relation for ultracool dwarfs.

Here we present simultaneous radio, X-ray, optical, and UV observations of one such system, the L dwarf binary 2MASSW J0746425+200032 (hereafter, 2M 0746+20). These observations are part of a long-term project to study the field properties of ultracool dwarfs (Berger et al. 2005, 2008a, 2008b). While no X-ray or UV emission are detected, the radio and Hα emission exhibit clear periodicity, which along with the known orbital inclination and $v \sin i$ allow us to explore for the first time the radius and magnetic field topology of an xs L dwarf.

2. OBSERVATIONS

2.1. Target Selection and Properties

We targeted the L dwarf binary 2M 0746+20 (L0+L1.5) due to the availability of its orbital parameters and rotation velocity, as well as previous detections in Hα. The binary is located at a distance of only 12.2 pc (Dahn et al. 2002), with a projected semi-major axis of about 0.2″ (Bouy et al. 2004). Thus, none of our observations detailed below (radio, optical, UV, and X-rays) spatially resolve the binary. The orbital inclination and total binary mass are $142 \pm 3^\circ$ and $0.146^{+0.016}_{-0.006}\ M_\odot$, respectively (Bouy et al. 2004). The rotation velocities quoted in the literature are 26 ± 3 km s^{-1} (Bailer-Jones 2004), 24 km s^{-1} (Reid et al. 2002), 31 km s^{-1} (Reiners & Basri 2008), and 28 km s^{-1} (C. Blake 2008, private communication), and we thus adopt an average value of $v \sin i = 27 \pm 3$ km s^{-1}. We note that the velocities are measured from the integrated light of the unresolved binary. However, since the primary contributes about 70% of the light (Bouy et al. 2004) we assign the measured $v \sin i$ to the primary. The bolometric luminosity of 2M 0746+20 is $L_{\rm bol} = 10^{-3.64 \pm 0.06}\ L_\odot$ (Vrba et al. 2004). We note that there is still no agreement as to whether the secondary member of the binary is a low-mass star or a brown dwarf (Bouy et al. 2004; Gizis & Reid 2006).

Previous Hα detections revealed an equivalent width range of $\approx$ 1.2–2.4 Å, or $\log(L_{\rm H\alpha}/L_{\rm bol}) \approx -5.3$ to -5.2 (Reid et al. 2000, 2002; Schmidt et al. 2007; Reiners & Basri 2008). No radio emission was previously detected at 8.46 GHz to a 3σ limit of $\lesssim 48\ \mu$Jy (Berger 2006), but subsequent to the observations presented here, Antonova et al. (2008) published a radio detection at 4.86 GHz with $F_\nu = 286 \pm 24\ \mu$Jy, based on a 2 hr observation. They further detect the possible emergence of a flare in the last few minutes of their observation.

The simultaneous observations presented here were conducted on 2008 February 22 UT for a total of 8.4 hr in the radio (02:11–10:34 UT), 8.83 hr in the X-rays (02:20–11:10 UT), and 7.4 hr in the optical (05:43–13:09 UT). Observations with the *Swift* UV/Optical Telescope (UVOT) took place intermittently between 01:32 and 09:54 UT with a total on-source exposure time of 2.15 hr.

2.2. Radio

Very Large Array[11] observations were obtained simultaneously at 4.86 and 8.46 GHz in the standard continuum mode with 2×50 MHz contiguous bands. Thirteen antennas were used at each frequency in the BnC array configuration. Scans of 295 s on source were interleaved with 55 s scans on the phase calibrator J0738+177. The flux density scale was determined using the extragalactic source 3C 286 (J1331+305). Data reduction and analysis follow the procedures outlined in Berger et al. (2008a) and Berger et al. (2008b). We detect a source coincident with the position[12] of 2M 0746+20 at both frequencies.

2.3. Optical Spectroscopy

We used[13] the Gemini Multi-Object Spectrograph (GMOS; Hook et al. 2004) mounted on the Gemini-North 8 m telescope with the B600 grating at a central wavelength of 5250 Å, and with a 1″ slit. The individual 300 s exposures were reduced using the `gemini` package in IRAF (bias subtraction, flat-fielding, and sky subtraction), and the wavelength solution was determined from CuAr arc lamps. The spectra cover 3840–6680 Å at a resolution of about 5 Å. A total of 77 exposures were obtained, with an on-source efficiency of 94%. We detect Hα emission in all the individual spectra.

2.4. X-Rays

Observations were performed with the Chandra/ACIS-S3 backside-illuminated chip for a total of 29.46 ks. The data were analyzed using CIAO version 3.4, and counts were extracted in a 2″ radius circle centered on the position of 2M 0746+20. We find only 2 counts, with 1.5 counts expected from the background as determined from annuli centered on the source position. Thus, the resulting upper limit is about 7 counts (95% confidence level). Using an energy conversion factor of 1 cps $= 3.8 \times 10^{-12}$ erg cm^{-2} s^{-1} (appropriate for a 1 keV Raymond-Smith plasma model in the 0.2–2 keV range) we find $F_X < 9.0 \times 10^{-16}$ erg cm^{-2} s^{-1}, or $L_X/L_{\rm bol} \lesssim 10^{-4.7}$.

2.5. Ultraviolet

Data were obtained with the *Swift*/UVOT in the UVW1 filter ($\lambda_{\rm eff} \approx 2600$ Å), as a series of 6 images with exposure times ranging from 460 to 1625 s. No source is detected at the position of 2M 0746+20 in any of the individual exposures or in the combined 2.15 hr image. Photometry of the combined image results in a limit of $F_\lambda < 2.8 \times 10^{-18}$ erg cm^{-2} s^{-1} Å^{-1} in a 2″ aperture. The ratio of UV to bolometric luminosity is $\lambda L_\lambda/L_{\rm bol} \lesssim 10^{-3.8}$.

3. MULTI-WAVELENGTH PERIODIC EMISSION

3.1. Radio Emission

The radio emission from 2M 0746+20 has an average flux density of $304 \pm 15\ \mu$Jy at 4.86 GHz, and $154 \pm 14\ \mu$Jy at 8.46 GHz. This is the first detection of the object at 8.46 GHz, with an increase by at least a factor of 3 compared to previous limits from 2002 June (Berger 2006). The average fraction of

[11] The VLA is operated by the National Radio Astronomy Observatory, a facility of the National Science Foundation operated under cooperative agreement by Associated Universities, Inc.

[12] We take into account the known proper motion of 370 mas yr^{-1} at a position angle of 264° (Schmidt et al. 2007).

[13] Observations were obtained as part of program GN-2008A-Q-11.

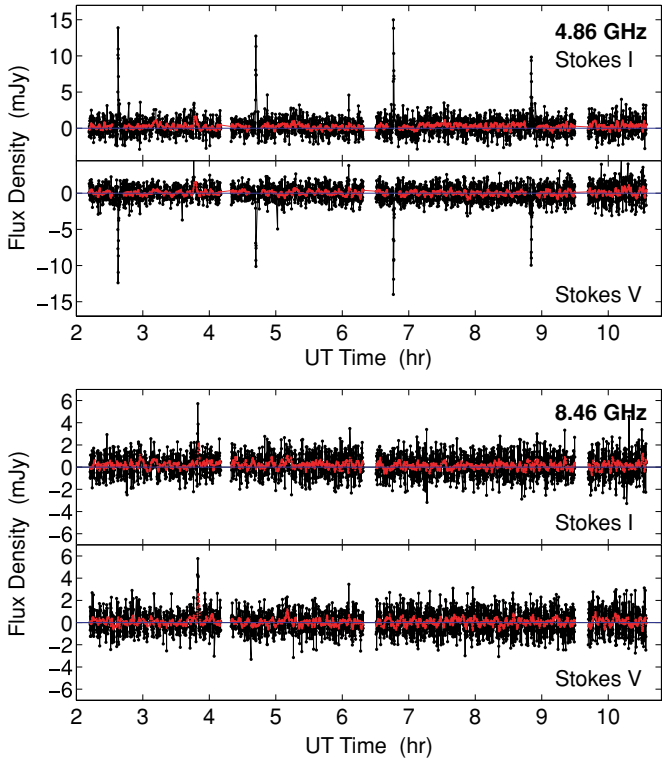

Figure 1. Radio light curves of 2M 0746+20 at 4.86 GHz (top) and 8.46 GHz (bottom) in stokes I (total intensity) and stokes V (circular polarization; negative values indicate left-handed polarization). The data are shown at the native 5 s time resolution (black points) and smoothed with a 1 minute boxcar (red points). The radio emission at 4.86 GHz is dominated by bright, $\sim$ 100% circularly polarized, and periodic bursts ($P = 124.32 \pm 0.11$ min), with no corresponding emission at 8.46 GHz. These properties point to coherent emission. In addition, we detect quiescent, nonvariable emission at both frequencies, with a spectral index indicative of gyrosynchrotron radiation.

(A color version of this figure is available in the online journal.)

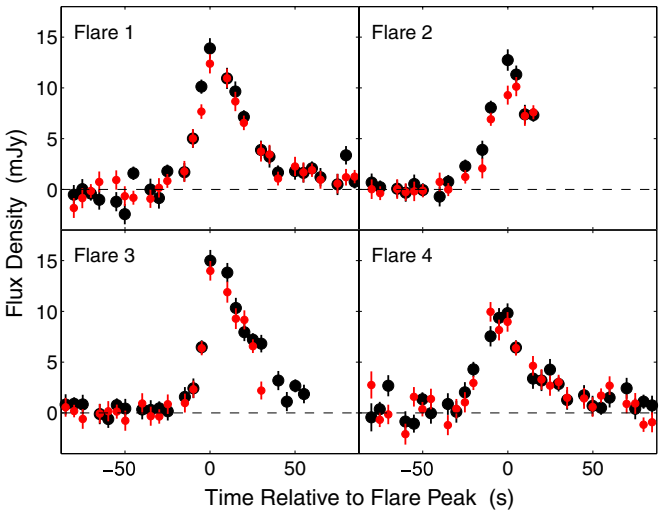

Figure 2. Zoom-in view on the four bursts detected at 4.86 GHz. Time is measured relative to the peak of each burst. Both total intensity (black) and circular polarization (red) are shown, with the latter inverted for ease of comparison. The bursts are nearly 100% circularly polarized. The rise time of the bursts is about 20 s, while the decay time is about 40 s.

(A color version of this figure is available in the online journal.)

circular polarization is $\lesssim 15\%$ (3σ) and $35 \pm 10\%$, respectively. The resulting average luminosities are $L_\nu(4.86) = (5.4 \pm 0.3) \times 10^{13}$ and $L_\nu(8.46) = (2.8 \pm 0.3) \times 10^{13}$ erg cm^{-2} s^{-1} Hz^{-1}, and the ratio relative to the bolometric luminosity is $\nu L_\nu / L_{\rm bol} \approx 10^{-6.55}$. These values are similar to those of previously detected late-M and L dwarfs (Berger 2006).

The radio light curves are shown in Figure 1. The most striking aspect of the radio emission is a set of bright (10–15 mJy), short duration (1.2 min), circularly polarized ($\sim$ 100%), and *periodic* pulses at 4.86 GHz. The period measured from the well-defined peaks[14] of the four detected pulses is 124.32 ± 0.11 min. No corresponding emission is detected at 8.46 GHz, indicating that the fractional bandwidth is $\delta\nu/\nu \lesssim 0.7$. The pulses are detected at both intermediate frequencies of the 4.86 GHz band (4885 MHz and 4835 MHz), with no clear time delay implying that $\delta\nu/\nu \gtrsim 0.02$.

The detailed temporal profiles of the pulses in total intensity and circular polarization are shown in Figure 2. The profiles are similar in all four cases, with a rise time of about 20 s, followed by a decline timescale of 40 s. The high degree of stability of the period and emission properties demonstrate that the pulsing activity is the result of stellar rotation, rather than genuine episodic flares. In this context, the duty cycle of only 0.8% implies that the radio emitting region has an azimuthal scale of only $\sim 0.1\ R_*$ (assuming a height above the surface of about 0.5–1 R_*; Hallinan et al. 2008). Furthermore, since the measured period roughly agrees with the rotation velocity of 2M 0746+20 (Section 2), we conclude that only one pulse is observed per rotation. Along with the uniform sense of circular polarization, this indicates that we observe only one of the magnetic poles.

The properties of the periodic pulses are similar to those observed in TVLM 513−46546 and LSR 1835+32 (Hallinan et al. 2007, 2008), and point to a coherent emission process, most likely the electron cyclotron maser (e.g., Treumann 2006). In this framework, the radiation is produced primarily at the electron cyclotron frequency, $\nu_c \approx 2.8 \times 10^6\ B$ Hz, indicating that the magnetic field strength of 2M 0746+20 in the radio emitting region is $B \approx 1.7$ kG. We can also place a limit on the electron density using the constraint that the plasma frequency, $\nu_p \approx 9 \times 10^3\ n_e^{1/2}$ Hz, has to be lower than ν_c. We thus find, $n_e \lesssim 3 \times 10^{11}$ cm^{-3}.

A single short-duration burst is also detected at 8.46 GHz (03:49:36 UT; Figure 1), with a peak flux of about 6 mJy, an identical duration to the 4.86 GHz pulses, and $\sim$ 100% right circular polarization. No corresponding emission is detected at 4.86 GHz. In the context of electron cyclotron maser emission, this burst requires a stronger magnetic field component of $B \approx 3$ kG. The burst is delayed by 72 min (or $0.58 \times P$) relative to the preceding 4.86 GHz pulse, indicating that its emission region is not trivially related to that of the periodic pulses. This, and the lack of periodicity, suggest that the 8.46 GHz burst is either the result of transitory field dissipation (a genuine flare), or that the physical conditions in its emission region (field strength and/or density) vary rapidly with time so as to suppress the emerging 8.46 GHz radiation during subsequent rotations. In either case, it is clear that the magnetic field strength ranges by at least a factor of 2 over the stellar surface and/or corona.

Eliminating the contribution of the short-duration pulses, we find baseline quiescent emission of 224 ± 15 μJy (4.86 GHz) and 149 ± 15 μJy (8.46 GHz) with no clear sign of variability (Figure 1). The quiescent emission is distinct from the narrow-

[14] The UT times of the four peaks are 02:37:37.6, 04:41:57.5, 06:46:07.3, and 08:50:37.7.

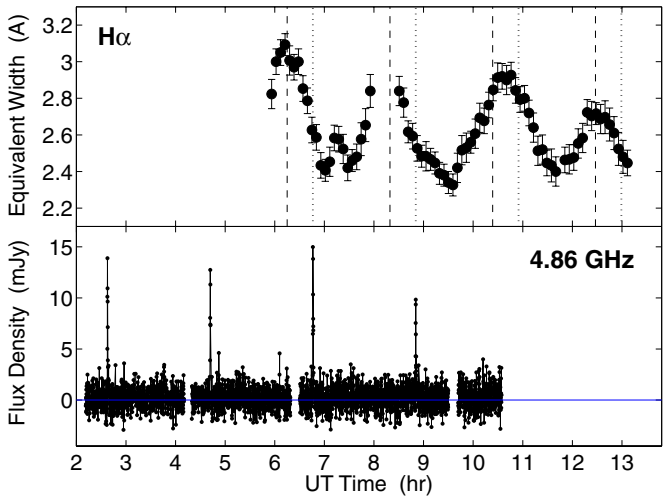

Figure 3. Hα equivalent width light curve (top) in comparison to the 4.86 GHz total intensity light curve (bottom). The Hα emission is clearly sinusoidal, with the same period as that measured from the radio bursts. The peaks of the Hα light curve (dashed lines) lead the radio bursts (dotted lines) by exactly 1/4 of a period. These properties, along with the nonzero minima, point to emission from a large-scale chromospheric structure whose projected solid angle varies with the rotation of 2M 0746+20.

(A color version of this figure is available in the online journal.)

band pulses since it is detected at both 4.86 and 8.46 GHz and it does not vary with the stellar rotation. The wide frequency range ($\delta\nu/\nu \sim 1$) and inferred spectral index of -0.7 ± 0.3 are typical of optically thin gyrosynchrotron emission from a power law distribution of electrons with an energy index of $p \approx 2.4$ (Güdel 2002). The lack of variability during 8.4 hr (or four rotations) suggests that the quiescent emission arises from particle acceleration in a uniform large-scale field component with order unity covering fraction.

3.2. Hα Emission

The Hα light curve is shown in Figure 3. The equivalent width ranges from 2.4 to 3.1 Å, with a mean value of about 2.7 Å. More importantly, the light curve is clearly periodic, with $P = 126 \pm 10$ min in excellent agreement with the radio periodicity. This indicates that the radio and Hα emission arise from the same binary member. However, despite the identical periods, two clear differences are present between the Hα and radio light curves, which provide additional constraints on the geometry of the magnetic field.

First, the Hα light curve is sinusoidal as opposed to the $\sim$ 1% duty cycle of the radio pulses. This indicates that the Hα emission is produced by chromospheric plasma that covers a substantial fraction (though less than 100%) of the stellar surface and rotates relative to our line of sight. A small enhancement is ruled out since it would result in a sharp rise and decline through ingress and egress, respectively, and a flat-topped peak. In addition, the nonzero minimum equivalent width (≈ 2.4 Å) indicates that the sinusoidal variations are most likely due to a combination of rotation and field orientation effects, such that at any given time some fraction of the Hα-emitting chromosphere is visible, with the maximum projected solid angle corresponding to the light-curve peaks (see Section 4).

Second, while the radio and Hα periods are identical, the phase of the two light curves differs (Figure 3). In particular, we find that the Hα peaks lead the radio pulses by about 31 min, corresponding to 1/4 of the period (or, equivalently 1/4 of a rotation). This lag indicates that the narrow beam which gives rise to the radio pulses is offset by about 90° relative to the central axis of the chromospheric geometry. As we show in the following section, such a 90° offset cannot be accommodated in a simple dipole magnetic field model, unless there is a significant breaking of the symmetry between the field and emission regions.

We have previously observed similar periodic Hα emission from the M8.5 dwarf TVLM 513−46546, with $P \approx 2$ hr well matched to the rotation velocity of $v \sin i \approx 60$ km s^{-1} (Berger et al. 2008a). This object has also been shown to produce radio bursts on a separate occasion (Hallinan et al. 2007). In the case of LSR 1835+32, on the other hand, despite the presence of periodic radio bursts (Hallinan et al. 2008) no periodic Hα emission was evident in a separate 5.4 hr observation (Berger et al. 2008b). It is thus possible that the magnetic field topology and stability timescale, as well as the viewing and magnetic axis orientation, play a role in determining the correlation (or lack thereof) between the periodic radio and Hα signals.

4. THE MAGNETIC FIELD GEOMETRY

Taking into account the properties of the radio and Hα emission, we now investigate the magnetic field topology. This topology has to satisfy the following requirements: (1) the Hα emission is due to a large-scale feature; (2) the nonzero minimum of the Hα light curve requires some fraction of the active chromosphere to be visible at all times; (3) the short-duration radio pulses arise from a narrow region; and (4) the radio pulses lag the Hα peaks by 1/4 of the period.

The first scenario we explore is a poloidal field with a simple dipole geometry. Such fields have been inferred for convective mid-M dwarfs, such as V374 Peg, from phase-resolved spectropolarimetry (Donati et al. 2006; Morin et al. 2008). This field geometry, and our line of sight orientation, are shown in Figure 4. We assume that the inclination of the rotation axis relative to our line of sight is identical to the orbital axis, $i = 142°$. In order to explain the radio pulses with a small duty cycle the magnetic axis has to be tilted relative to the rotation axis so that the beam emerging from the radial field at the poles sweeps into out line of sight once per rotation (a "pulsar configuration"). This configuration also explains the Hα modulation since the solid angle subtended by the poloidal field that is projected along our line of sight varies sinusoidally as the object rotates. Specifically, as the field is tilted towards our line of sight we observe maximum Hα emission (see panels A and B of Figure 4 for the geometry corresponding to the maximum and minimum Hα emission, respectively).

Unfortunately, while this simple model explains both the radio pulsations and the Hα light curve, it predicts a 1/2 phase lag between the two light curves, rather than the observed 1/4 phase lag. This is simply because the same phase of the rotation that orients the magnetic pole toward our line of sight (resulting in a radio burst), also projects the minimum solid angle of the dipole field (i.e., minimum Hα emission). This effect is independent of our choice of orbital inclination (Figure 4).

Alternatively, a toroidal dipole configuration, with the polar caps producing the brightest Hα emission, will also produce radio bursts and sinusoidal Hα emission. However, in this configuration the two light curves would be exactly in phase since when the polar region is oriented toward our line of sight we will observe both an enhancement of the Hα emission and a radio pulse.

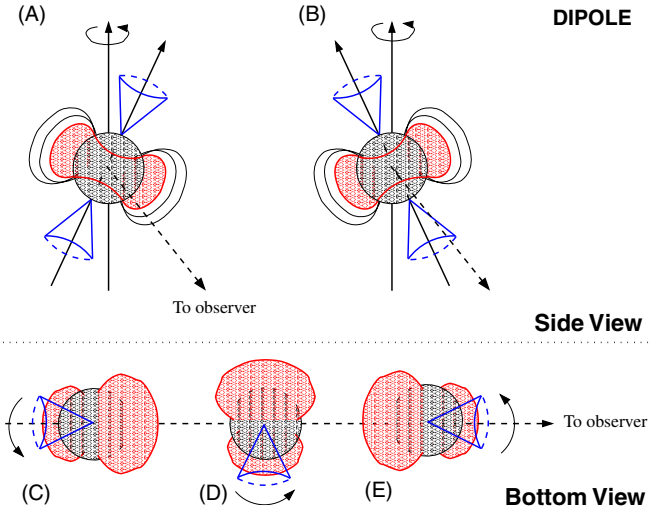

Figure 4. Dipole poloidal field topology for 2M 0746+20, and its orientation relative to the line of sight. This configuration leads to radio bursts (blue) and sinusoidal Hα emission (red). The top panels show a side view projection with the rotation axis inclined by 142○ relative to our line of sight (Section 2). Panel A represents the peak projected chromospheric emission region, and hence a peak in the Hα light curve, while panel B (1/2 rotation period later) represents the detection of a radio pulse coinciding with a minimum in the Hα light curve. The bottom panels show a bottom view projection of the same field configuration corresponding to a peak in the Hα light curve (C), an intermediate Hα flux (D: 1/4 rotation later), and a minimum in the Hα light curve coinciding with a radio pulse (E: 1/2 rotation later). From both projections it is clear that we expect a 1/2 phase lag between the two bands, with the minimum projected solid angle of the field (i.e., minimum Hα emission) coinciding with the radio bursts. In the alternative toroidal configuration, the Hα and radio peaks will be aligned since both are produced in the same polar region.

(A color version of this figure is available in the online journal.)

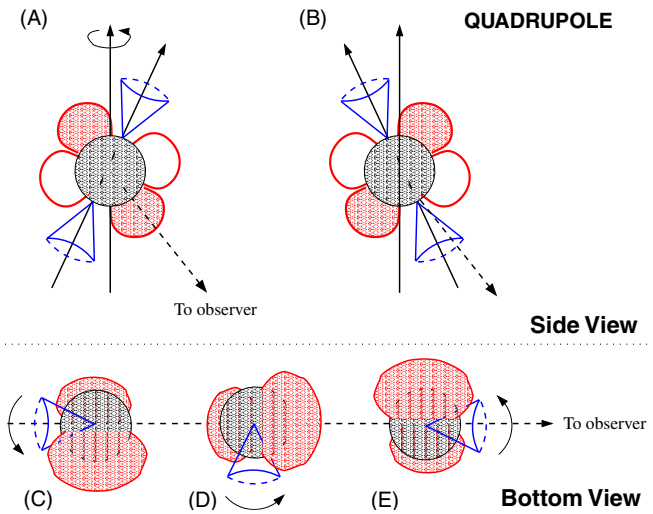

Figure 5. Same as Figure 4, but for a quadrupole field configuration. The individual panels correspond to the same orbital phase as in Figure 4. Shaded red regions correspond to bright Hα hot spots, while empty regions correspond to little or no Hα emission. In this configuration, there is a 1/4 phase lag between the peak Hα and radio emission (panels D and E, respectively), and it thus reproduces both the light-curve shapes and the 1/4 phase lag. However, this configuration requires nonuniform Hα surface brightness, with two of the quadrupole lobes (on opposite hemispheres) producing stronger Hα emission.

(A color version of this figure is available in the online journal.)

Having rejected the simple dipole poloidal and toroidal configurations, we are left with two possibilities to explain the 1/4 phase lag and the radio/Hα light curves. First, the magnetic field configuration is more complex and dominated by higher order multipoles. Or second, there is a breaking of the symmetry either in the alignment between the poles and radio pulses, or between the poloidal/toroidal structure and the Hα emission. In the former case, the simplest possibility is that the field is quadrupolar, leading naturally to the possibility of a 1/4 phase lag (as opposed to 0 or 1/2 phase lag for the dipole field). However, the quadrupole cannot produce uniform Hα emission since this would result in a nonvarying light curve. Instead, two of the quadrupole "lobes" have to produce enhanced Hα emission—for example, one each in the northern and southern hemispheres. This configuration is shown in Figure 5, and it appears to explain all of the available observations.

The alternative hypothesis of symmetry breaking can accommodate several possibilities. In the simplest scenario, the radio emission does not emerge uniformly from the polar caps, but is instead produced in a localized region at lower latitude (a "hot-spot configuration"). As the object rotates the hot-spot moves in and out of our line of sight. This may work in both the toroidal and poloidal dipole configurations, since both can explain the sinusoidal Hα variability. However, the arbitrary location of the hot spot does not trivially explain the exact 1/4 phase lag observed here.

More complex possibilities exist for both the high-order multipole scenario and the broken symmetry scenario. However, the stability of the radio pulses and the overall smooth Hα light curve suggest that the dominant topology is not significantly more complex than the scenarios we explored here.

To summarize, we find that the 1/4 phase lag between the radio and Hα light curves eliminates simple and symmetric dipole field configurations in which the radio emission is produced at the poles, and the Hα emission arises from plasma confined by the dipole field; in this configuration we expect the phase lag to be either zero (toroidal field) or 1/2 (poloidal field). The simplest alternative is to either: (1) retain the polar origin of the radio emission, but appeal to a quadrupole field with nonuniform Hα emission; or (2) retain the dipole configuration as the origin of the Hα emission, but shift the location of the radio emission from the poles to a hot spot at lower latitude. We finally note that in any of the possible configurations, the quiescent nonvariable radio emission is likely produced by the largest scale field structure, such that the projection effects caused by the rotation and magnetic axis tilt are minimized.

The possible field topologies that give rise to the observed radio and Hα emission appear to be somewhat more complex than those inferred for mid-M dwarfs from spectropolarimetric observations (Donati et al. 2006; Morin et al. 2008). Zeeman–Doppler imaging points to predominantly dipole poloidal fields, particularly for objects with the lowest Rossby numbers, $\mathrm{Ro} \equiv P/\tau_c \lesssim 0.05$, ($\tau_c$ is the convective overturn timescale). For 2M 0746+20 we estimate $\tau_c \approx (MR^2/L)^{1/3} \approx 200$ d (Section 5), so the inferred Rossby number is extremely small, $\mathrm{Ro} \approx 4 \times 10^{-4}$, and we may have expected the dipole poloidal configuration to dominate. Thus, our observations indicate that the field topology possibly evolves from mid-M dwarfs to L dwarfs, and that Ro may not be the only relevant parameter.

5. THE MASS–RADIUS RELATION

We next use the rotation period as determined from the radio and Hα emission to infer the stellar radius. Since we do not spatially resolve the binary in our observations, we assume that the radio and Hα emission arise from the more luminous

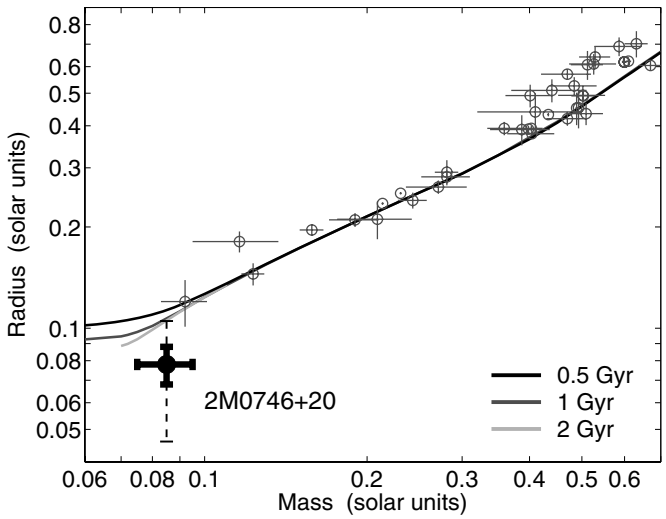

Figure 6. Stellar radius as a function of mass for the primary star in 2M 0746+20. Also shown are model tracks (Baraffe et al. 1998) for stellar ages of 0.5, 1, and 2 Gyr, as well as a compilation of higher mass stars (open symbols; López-Morales 2007). The inferred radius of 2M 0746+20a is about 30% smaller than predicted by the models, with the smallest discrepancy for the oldest age. The overall disagreement indicates either a problem with the evolutionary models near the bottom of the main sequence, or that our assumption that the rotation and orbital inclinations are identical is wrong. The dashed line indicates the range of inferred radii that corresponds to the minimum allowed radius (i.e., $i = 90°$) and the 90% inclination probability (i.e., there is $< 10\%$ probability that the inclination angle is such that the inferred radius will be larger than this value). This latter value is marginally consistent with the theoretical models.

primary. Since the measured rotation velocity applies to the primary as well (Section 2), this allows us to infer its radius. We further make the reasonable assumption that the inclination of the rotation axis, i, is identical to the orbital orientation of $142 \pm 3°$ (Hale 1994). Thus, the projected $v \sin i = 27 \pm 3$ km s^{-1} translates to an actual rotation velocity of $v = 46 \pm 6$ km s^{-1}. For a period of 124.32 ± 0.11 min, the corresponding radius of 2M 0746+20 is $R = (5.4 \pm 0.7) \times 10^9$ cm, or 0.078 ± 0.010 $R_\odot$. As far as we know, this is the first radius estimate (without a $\sin i$ degeneracy) for an L dwarf through photometric variability.

The total mass of the binary, inferred by Bouy et al. (2004) from the orbital dynamics, is $0.146^{+0.016}_{-0.006}$ $M_\odot$. These authors further estimated a range of 0.075–0.095 $M_\odot$ for the primary by comparing the infrared photometry with DUSTY model isochrones. Gizis & Reid (2006), on the other hand, argued that the primary mass is 0.078–0.082 $M_\odot$, primarily as a result of an older age for the system. Taking the conservative approach, we adopt here the wider range of values from Bouy et al. (2004).

The inferred radius and mass are plotted in Figure 6. Also shown are the mass–radius relations from the evolutionary models of Baraffe et al. (1998) for ages of 0.5, 1, and 2 Gyr and solar metallicity, as well as masses and radii for stars in the range 0.1–0.7 $M_\odot$ from a recent compilation by López-Morales (2007). 2M 0746+20a lies below the model predictions, $R \approx 0.105$–0.115 $R_\odot$, by about 30%. This is surprising since stars with known radii in the mass range 0.1–0.3 $M_\odot$ appear to generally agree with the model predictions (López-Morales 2007). Moreover, stars in the mass range 0.4–0.7 $M_\odot$ generally lie above the model predictions, possibly as a result of magnetic activity (López-Morales 2007). It is somewhat surprising then, that a highly active L dwarf would underlie the same theoretical models. Similarly, a recent estimate of $R \gtrsim 0.117$ $R_\odot$ for the M8.5 dwarf LSR 1835+32 (Hallinan et al. 2008), based on similar periodic radio emission to that of 2M 0746+20, indicates that there is possibly a larger than expected dispersion in the radii of ultracool dwarfs.

With only a single object it is impossible to assess whether the apparent discrepancy indicates that the theoretical models break down across the substellar boundary, or if this is the result of our assumption that the rotation axis is aligned with the orbital inclination. It is unlikely that the problem is with the value of $v \sin i$ since several groups have measured consistent values (Section 2). If we relax our assumption of $i = 142°$, then the minimum allowed radius (corresponding to $i = 90°$) is 0.046 $R_\odot$. The radius corresponding to the 90% probability of the inclination axis distribution ($i > 26°$) is $R \approx 0.105$ $R_\odot$ (i.e., there is only a 10% probability that $R > 0.105$ $R_\odot$). This latter value is marginally consistent with the theoretical predictions, but it requires the rotation axis to be severely misaligned with the orbital inclination.

6. SUMMARY AND CONCLUSIONS

We presented simultaneous radio, X-ray, optical, and UV observations of the L dwarf binary 2M 0746+20. Both the radio and Hα light curves are dominated by periodic emission, with $P \approx 124$ min. The agreement between the two periods indicates that both arise from the same binary member, which we assume to be the primary star. We note that high angular resolution Very Long Baseline Array observations may pinpoint the origin of the radio emission.

The observed period is well matched to the rotation velocity of 2M 0746+20, and the assumption that the rotation axis is aligned with the orbital inclination allows us to infer a radius of $R = 0.078 \pm 0.010$ $R_\odot$. Combined with the estimated mass of 0.085 ± 0.010 $M_\odot$ (Bouy et al. 2004), we find that the radius is about 30% smaller than predicted from theoretical evolutionary models. It is unclear from this single object whether this is the result of a breakdown in the models, or an indication that the rotation and orbital axes are severely misaligned. Both possibilities have important implications for our understanding of ultracool dwarfs and their formation mechanism.

The combination of periodic radio and Hα emission further allows us to explore the magnetic field topology. The radio periodicity is in the form of short-duration pulses with a duty cycle of 0.8% and a uniform sense of circular polarization, while the Hα emission is sinusoidal and leads the radio emission by 1/4 of a phase. These emission properties can be explained in the context of a rotating misaligned magnetic field, but the observed phase lag rules out a symmetric dipole field. Instead, we conclude that either the field is dominated by a quadrupole configuration, or the emission regions are not trivially aligned with a dipole field. In both scenarios the quiescent and nonvariable radio emission most likely arises from the largest scales of the field, which are least affected by rotation and inclination effects.

We note that the availability of simultaneous radio and optical data is crucial to our understanding of the field geometry. If only one band was available to us (as in all previous cases of detected radio pulses), we would have concluded that the dipole topology is the most likely scenario. Instead, the field configuration of 2M 0746+20 appears to be somewhat more complex than those inferred for mid-M dwarfs from phase-resolved optical spectropolarimetry (Donati et al. 2006; Morin et al. 2008), although the vast difference in techniques may result in sensitivity to different field structures. Regardless of

the exact configuration, our observations support the general conclusions of recent numerical dynamo simulations (Browning 2008), which predict large-scale fields at low Rossby numbers. Indeed, we estimate that the Rossby number for 2M 0746+20 is very low, $\sim 4 \times 10^{-4}$.

Future observations of 2M 0746+20 will allow us to determine the stability timescale of the magnetic field configuration, a crucial constraint on dynamo models. Previous observations of the L3.5 dwarf 2M 0036+18 (Berger et al. 2005; Hallinan et al. 2008) indicated stability on a timescale of at least ~ 3 yr. In addition, continued surveys for radio emission from low-mass stars and brown dwarfs, particularly in binary systems, are warranted. As demonstrated here, these observations, particularly in conjunction with optical spectroscopy, can provide important constraints not only on the mass–radius relation below $\sim 0.1\ M_{\odot}$, but also on the magnetic field topology of fully convective objects.

We thank the *Chandra*, Gemini, VLA, and *Swift* schedulers for their invaluable help in coordinating these observations. This work has made use of the SIMBAD database, operated at CDS, Strasbourg, France. It is based in part on observations obtained at the Gemini Observatory, which is operated by the Association of Universities for Research in Astronomy, Inc., under a cooperative agreement with the NSF on behalf of the Gemini partnership: the National Science Foundation (United States), the Science and Technology Facilities Council (United Kingdom), the National Research Council (Canada), CONICYT (Chile), the Australian Research Council (Australia), CNPq (Brazil) and CONICET (Argentina). Data from the UVOT instrument on *Swift* were used in this work. *Swift* is an international observatory developed and operated in the US, UK and Italy, and managed by NASA Goddard Space Flight Center with operations center at Penn State University. Support for this work was provided by the National Aeronautics and Space Administration through Chandra Award Number G08-9013A issued by the *Chandra X-ray Observatory* Center, which is operated by the Smithsonian Astrophysical Observatory for and on behalf of the National Aeronautics Space Administration under contract NAS8-03060.

REFERENCES

Antonova, A., Doyle, J. G., Hallinan, G., Bourke, S., & Golden, A. 2008, A&A, 487, 317
Antonova, A., Doyle, J. G., Hallinan, G., Golden, A., & Koen, C. 2007, A&A, 472, 257
Audard, M., Osten, R. A., Brown, A., Briggs, K. R., Guedel, M., Hodges-Kluck, E., & Gizis, J. E. 2007, A&A, 471, L63
Bailer-Jones, C. A. L. 2004, A&A, 419, 703
Baraffe, I., Chabrier, G., Allard, F., & Hauschildt, P. H. 1998, A&A, 337, 403
Berger, E. 2002, ApJ, 572, 503
Berger, E. 2006, ApJ, 648, 629
Berger, E., et al. 2001, Nature, 410, 338
Berger, E., et al. 2005, ApJ, 627, 960
Berger, E., et al. 2008a, ApJ, 673, 1080
Berger, E., et al. 2008b, ApJ, 676, 1307
Bouy, H., et al. 2004, A&A, 423, 341
Browning, M. K. 2008, ApJ, 676, 1262
Burgasser, A. J., & Putman, M. E. 2005, ApJ, 626, 486
Dahn, C. C., et al. 2002, AJ, 124, 1170
Donati, J.-F., Forveille, T., Cameron, A. C., Barnes, J. R., Delfosse, X., Jardine, M. M., & Valenti, J. A. 2006, Science, 311, 633
Gizis, J. E., & Reid, I. N. 2006, AJ, 131, 638
Güdel, M. 2002, ARA&A, 40, 217
Hale, A. 1994, AJ, 107, 306
Hallinan, G., Antonova, A., Doyle, J. G., Bourke, S., Brisken, W. F., & Golden, A. 2006, ApJ, 653, 690
Hallinan, G., Antonova, A., Doyle, J. G., Bourke, S., Lane, C., & Golden, A. 2008, ApJ, 684, 644
Hallinan, G., et al. 2007, ApJ, 663, L25
Hook, I. M., Jørgensen, I., Allington-Smith, J. R., Davies, R. L., Metcalfe, N., Murowinski, R. G., & Crampton, D. 2004, PASP, 116, 425
López-Morales, M. 2007, ApJ, 660, 732
Morin, J., et al. 2008, MNRAS, 390, 567
Osten, R. A., Hawley, S. L., Bastian, T. S., & Reid, I. N. 2006, ApJ, 637, 518
Phan-Bao, N., Osten, R. A., Lim, J., Martín, E. L., & Ho, P. T. P. 2007, ApJ, 658, 553
Reid, I. N., Kirkpatrick, J. D., Gizis, J. E., Dahn, C. C., Monet, D. G., Williams, R. J., Liebert, J., & Burgasser, A. J. 2000, AJ, 119, 369
Reid, I. N., Kirkpatrick, J. D., Liebert, J., Gizis, J. E., Dahn, C. C., & Monet, D. G. 2002, AJ, 124, 519
Reiners, A., & Basri, G. 2006, ApJ, 644, 497
Reiners, A., & Basri, G. 2007, ApJ, 656, 1121
Reiners, A., & Basri, G. 2008, ApJ, 684, 1390
Schmidt, S. J., Cruz, K. L., Bongiorno, B. J., Liebert, J., & Reid, I. N. 2007, AJ, 133, 2258
Treumann, R. A. 2006, A&AR, 13, 229
Vrba, F. J., et al. 2004, AJ, 127, 2948